Generation of arbitrary lithographic patterns using Bose-Einstein-condensate interferometry

M. F. Fouda, R. Fang, J. B. Ketterson, and M. S. Shahriar

Phys. Rev. A **94**, 063644 — Published 28 December 2016

DOI: 10.1103/PhysRevA.94.063644

Generation of Arbitrary Lithographic Patterns Using BEC Interferometry

M.F. Fouda[1], R. Fang[2], J. B. Ketterson[2] and M.S. Shahriar[1,2]
[1]Department of EECS, Northwestern University, Evanston, IL 60208, USA
[2]Department of Physics and Astronomy, Northwestern University, Evanston, IL 60208, USA

Abstract

We propose an arbitrary pattern lithography process using interference of Bose-Einstein Condensates (BEC). A symmetric three pulse Raman atom interferometer (AI) is used to implement the system. The pattern information, in the form of a phase-only mask, is optically encoded into the BEC order parameter in one of the AI arms. The lithographic pattern is represented by a two-dimensional intensity variation, and is transformed into a two-dimensional phase variation in the BEC order parameter via the use of AC-stark shift induced by a pulsed laser field. The BEC probability distribution of the interference result at the end of the AI is proportional to the required pattern. In order to produce features smaller than the diffraction limit for the used optical elements, we employ a three-dimensional atomic lens system to scale down the resulting pattern. The operating conditions for this lens structure are investigated in order to identify practical constraints. Simulations of the overall system using the parameters of ^{87}Rb BEC were performed to illustrate its functionality. The proposed process, while perhaps not suitable for general purpose usage, may enable the creation of special purpose patterns on a very small scale, with features as small as few nanometers.

PACS Numbers: 03.75.Hh, 03.75.Dg, 81.16.Nd, 32.60.+i

I. Introduction

Recent years have witnessed extensive research for new lithographic processes. The current industrial lithography systems are expected to be unable to address future challenges. The electronics industry is looking for parallel lithography techniques that are capable of generating patterns with the length scale of few nanometers. Current optical lithography systems cannot reach this length scale because of diffraction limit.

Multiple approaches have been pursued to go beyond these limits by using atoms for lithography. One of the earliest works in this field [1] made use of the intensity-dependent force exerted by nearly resonant light on neutral two-level atoms to generate submicron lithographic patterns. In this work, a standing wave was used to manipulate a Sodium atomic beam to create a grating with period equal to half the wavelength of the standing light wave. This approach was later extended to create parallel lines of Chromium on a Silicon substrate [2]. Generation of two dimensional patterns followed [3, 4] by using multiple standing waves to create two dimensional grating patterns. Multiple efforts targeted the minimization of the feature size obtained by this approach [5, 6]. Although the spacing between features is generally set by half the wavelength of the standing wave, some efforts show that it is possible to go beyond that limit [6, 7].

Unfortunately, this approach does not allow the generation of arbitrary two dimensional patterns. The work in [8] suggested an approach for circumventing this constraint by frequency encoding the pattern information in the light mask instead of using intensity encoding. The resolution obtained by this technique was barely below the single micrometer scale.

In this paper, we propose an arbitrary pattern nano-lithography system using interferometry of Bose Einstein Condensates (BECs). Atomic interferometry using BEC has been demonstrated under various configurations [9-11], thus paving the way for the feasibility of the concept being proposed here. We had previously proposed an arbitrary pattern nano-lithography system [12] based primarily on the interference of individual atoms. This proposal had several limitations. First, while it alluded to the need for using a BEC to achieve a significant speed-up in the writing process, no details were presented on how the architecture and components would have to be modified for the BEC version. Second, the simulations were based on two-dimensional wave packets, ignoring the effect of the finite spatial extent in the third dimension. The analysis presented here addresses these two aspects in significant detail. Specifically, instead of using the linear Schrodinger equation -as was done in reference [12]- we use the nonlinear Gross-Pitaevskii equation as needed for modeling the evolution of a BEC order parameter. Second, we take into account the fact that the spatial extent of the BEC order parameter has a finite size in all three dimensions. We find that these considerations pose significant constraints on the design proposed in reference [12], leading to major modifications of the overall scheme. We also investigate the effect of various parameters on the fidelity of the lithographic reproduction process. In particular, we show that a very small scattering length, achievable possibly by the use of Feshbach resonance, is necessary for high quality reproduction of a desired pattern. We also show how the number of atoms in the condensate as well as the initial size of the order parameter affect the performance of the lithography system.

II. System structure

The basic tool for the proposed atom lithography system is the three pulse atom interferometer (AI) which was first theoretically proposed by Borde [13] and experimentally demonstrated by Kasevich and Chu [14]. In our proposed system, we use a symmetric Mach-Zehnder AI [15, 16]. In this structure -shown in Figure 1- a BEC is prepared in the ground state $|1\rangle$ and is moving in the z direction. When it encounters the $\pi/2$ pulse, it splits mainly into two components: state $|1\rangle$ and state $|3\rangle$. The later state has additional momentum in the y direction which causes it to split from state $|1\rangle$. Both components then encounter the π pulse which causes each packet to change its direction. The component in the AI upper arm is then modified by adding a spatially varying phase $\phi(x,y)$ which contains the lithographic pattern information. This process is performed using a detuned pulse of light with spatially varying intensity. The details of the phase modification process are discussed later.

After phase imprinting, a lens system - also realized by a detuned pulse of light - can be used to suppress the spreading of the BEC packet as well as to reduce its spatial extent. To keep the BEC components in both AI arms in spatial proportion, the lens system is replicated on the lower arm.

At the end of the AI, a final π/2 pulse is used to merge the BEC components from both arms. Due to the phase modification of the upper arm, the interference result will be proportional to the required lithographic pattern. The resulting interference result goes through another lens system to suppress distortion and then deposited onto a substrate to realize the pattern.

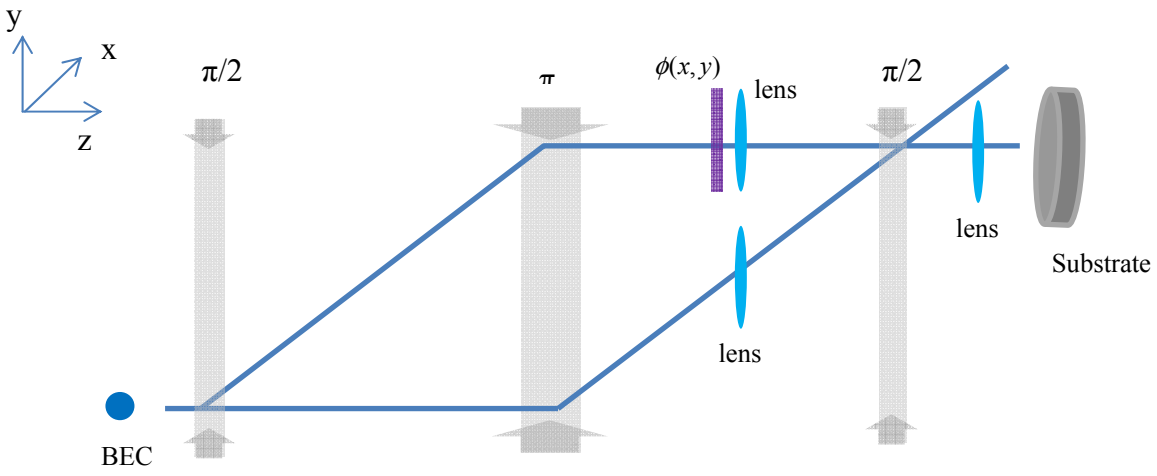

Figure 1. Architecture of 2D lithography system using BEC. See text for details.

III. Mathematical Analysis of the System

In this work, we only consider the case when the interaction between the atoms in the BEC is very small. The dynamics of the BEC can then be described by the time dependent Gross-Pitaevskii equation [17]

$$i\hbar\frac{\partial\psi(\vec{r},t)}{\partial t}=(-\frac{\hbar^2}{2m}\nabla^2+V(\vec{r},t)+U_0N\left|\psi(\vec{r},t)\right|^2)\psi(\vec{r},t). \qquad (1)$$

Here, $\psi(\vec{r},t)$ is the order parameter, $\vec{r}$ is the coordinate of the center of mass of the condensate, m is the mass of a single atom, $V(\vec{r},t)$ is the external potential, N is the number of BEC atoms and U_0 represents the interaction between the atoms, given by

$$U_0=\frac{4\pi\hbar^2a_s}{m}, \qquad (2)$$

where a_s is the scattering length.

In this system we assume that the condensate will propagate through the three zone atomic interferometer without confinement. Hence, during the Raman interaction the potential $V(\vec{r},t)$ is only due to the electric dipole interaction with the light field. During the dark zones, the condensate will propagate in free space with $V(\vec{r},t)=0$, except when it encounters the light pulses that represent the pattern and the lenses.

At the beginning of the AI, we assume that the BEC is in the ground state. We assume that the BEC source is prepared to have a low interaction energy compared to the BEC kinetic energy, as

in [18]. In this case, it is appropriate to express the BEC ground state order parameter to have a Gaussian profile in the x, y and z directions [19-22].

$$\psi_1(\vec{r},t=0)=\frac{1}{\sqrt{\sigma_x\sigma_y\sigma_z\sqrt{\pi^3}}}\exp(-\frac{x^2}{2\sigma_x^2})\exp(-\frac{y^2}{2\sigma_y^2})\exp(-\frac{z^2}{2\sigma_z^2}) \qquad (3)$$

The internal states of the atoms composing the condensate play a critical role in the splitting, redirecting and merging of the BEC packets inside the AI. The atoms are modeled as a three level Λ system as shown in Figure 2. Considering the internal atomic states, the BEC order parameter can be expressed as

$$\begin{aligned}\psi(\vec{r},t)&=C_1(t)\left|\psi_1(\vec{r},t)\right\rangle\left|1\right\rangle+C_2(t)\left|\psi_2(\vec{r},t)\right\rangle\left|2\right\rangle+C_3(t)\left|\psi_3(\vec{r},t)\right\rangle\left|3\right\rangle\\&=\tilde{c}_1(r,t)\left|1\right\rangle+\tilde{c}_2(r,t)\left|2\right\rangle+\tilde{c}_3(r,t)\left|3\right\rangle\end{aligned}. \qquad (4)$$

Here, $C_1(t)$, $C_2(t)$ and $C_3(t)$ represent the fraction of the BEC atoms in each internal state. The normalization condition of the order parameter requires that

$$\sum_{i=1}^{3}\left|C_i(t)\right|^2=\sum_{i=1}^{3}\left|\tilde{c}_i(\vec{r},t)\right|^2=1. \qquad (5)$$

For ^{87}Rb atoms, we chose state $\left|1\right\rangle$ to correspond to level $5^2S_{1/2}$ with $(F=1,\ m_F=1)$, state $\left|2\right\rangle$ to correspond to level $5^2P_{1/2}$ with $(F'=2,\ m_F=0)$ and state $\left|3\right\rangle$ to correspond to level $5^2S_{1/2}$ with $(F=2,\ m_F=-1)$.

Initially, all atoms are assumed to be in state $\left|1\right\rangle$. Hence, $C_1(t=0)=1,\ C_2(t=0)=0,\ C_3(t=0)=0$.

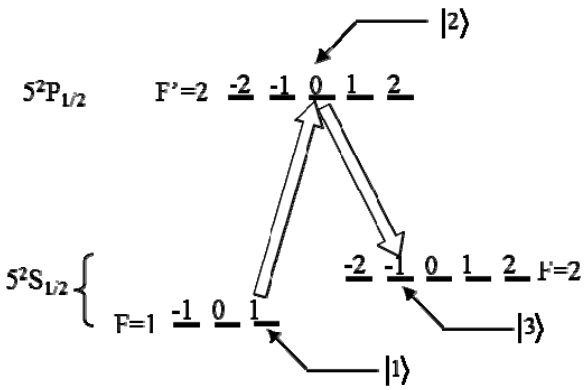

Figure 2. Three level system used by the atom interferometer. See text for details.

A. Free space propagation of BEC

Due to the nonlinear term in the GPE equation, it is difficult to study the BEC time evolution analytically. As such, we use numerical methods to calculate the condensate time evolution. In our simulation, explicit finite difference method is used to calculate time evolution. Forward difference is used for the time derivatives and central difference is used for the spatial derivatives.

$$\frac{\partial \psi}{\partial t} \to \frac{\psi_{t+\Delta t}^{x,y,z} - \psi_t^{x,y,z}}{\Delta t}, \frac{\partial^2 \psi}{\partial x^2} \to \frac{\psi_t^{x+\Delta x,y,z} - 2\psi_t^{x,y,z} + \psi_t^{x-\Delta x,y,z}}{(\Delta x)^2}$$
$$\frac{\partial^2 \psi}{\partial y^2} \to \frac{\psi_t^{x,y+\Delta y,z} - 2\psi_t^{x,y,z} + \psi_t^{x,y-\Delta y,z}}{(\Delta y)^2}, \frac{\partial^2 \psi}{\partial z^2} \to \frac{\psi_t^{x,y,z-\Delta z} - 2\psi_t^{x,y,z} + \psi_t^{x,y,z+\Delta z}}{(\Delta z)^2} \quad (6)$$

Here, Δx , Δy and Δz are the numerical grid resolution in the three spatial coordinates and Δt is the time step used. Using these approximations in equation (1), an iterative algorithm is implemented to calculate the time evolution of the BEC order parameter.

B. Interaction of BEC with the AI π and π/2 pulses

For the three-zone Raman AI, light field interaction is the mechanism to split the condensate into two separate paths, redirect the separated components and to merge them at the end of the AI. Light interaction changes the internal state of the wave packet. In this section, we study how the BEC order parameter interacts with the AI light fields. The goal here is to reach a mathematical form that can be used for the simulation of the electromagnetic interaction in the spatial domain. The details of the mathematical derivation are shown in Appendix A. The time evolution of the BEC internal states during laser field interaction is given by

$$\begin{aligned}
i\hbar\frac{\partial}{\partial t}c_1(r,t) &= \left(-\frac{\hbar^2}{2m}\nabla^2 + U_0\left|c_1(r,t)\right|^2\right)c_1(r,t) + \frac{\hbar\Omega_A}{2}e^{-ik_A y}c_2(r,t) \\
i\hbar\frac{\partial}{\partial t}c_2(r,t) &= \left(-\frac{\hbar^2}{2m}\nabla^2 + U_0\left|c_2(r,t)\right|^2 - \hbar\delta_1\right)c_2(r,t) + \frac{\hbar\Omega_A}{2}e^{ik_A y}c_1(r,t) + \frac{\hbar\Omega_B}{2}e^{-ik_B y}c_3(r,t) \quad (7) \\
i\hbar\frac{\partial}{\partial t}c_3(r,t) &= \left(-\frac{\hbar^2}{2m}\nabla^2 + U_0\left|c_3(r,t)\right|^2 + \hbar(\delta_2 - \delta_1)\omega_3\right)c_3(r,t) + \frac{\hbar\Omega_B}{2}e^{ik_B y}c_2(r,t)
\end{aligned}$$

With the ability to calculate the time evolution in free space and the ability to calculate the order parameter interaction with light fields, the evolution through the AI can be modeled numerically.

C. Imprinting a spatially varying phase shift

AC-stark shift – which is also called light shift – is used to imprint the lithographic pattern information on the BEC wave packet. This technique of quantum phase engineering has been demonstrated for BEC [23, 24]. AC-stark shift is due to a detuned light-matter interaction. For an atom in state $|1\rangle$, an AC field that couples states $|1\rangle \leftrightarrow |2\rangle$ will cause an energy shift of state $|1\rangle$. This energy shift is given by $\hbar\Omega^2/4\delta$ [25], where Ω is the Rabi frequency and δ is the detuning. The energy shift leads to a phase shift given by $\int_0^\tau (\Omega^2/4\delta)d\tau$, where τ is the interaction time. For nearly constant values of Ω and δ, the phase shift can be approximated as $(\Omega^2/4\delta)\tau$. As the Rabi frequency Ω is proportional to the electric field of the interacting light, the added phase is proportional to the intensity thereof. By controlling this intensity, it is possible to introduce any required phase shift to the BEC order parameter. The intensity of the phase modulating light pulse can be controlled by using a spatial light modulator (SLM), for example, as shown in Figure 3.

In order to determine the required intensity modulation to generate a specific lithographic pattern, we can consider a simple case where the BEC is split into two identical components. If a spatially varying phase shift $\phi(\vec{r})$ is added to only one of these components, the interference result can be expressed as $\psi_f(\vec{r}) = \psi_1(\vec{r}) + \psi_2(\vec{r}) = \psi(\vec{r})[1 + \exp(-i\phi(\vec{r}))] = 2\psi(\vec{r})\exp(-i\phi(\vec{r})/2)\cos(\phi(\vec{r})/2)$. The corresponding probability distribution can be written as $P_f(\vec{r}) = |\psi_f(\vec{r})|^2 = 2|\psi(\vec{r})|^2[1 + \cos(\phi(\vec{r}))]$. To ensure that the final interference result is proportional to the required lithographic pattern $F(\vec{r})$, the phase $\phi(\vec{r})$ is chosen to be $\phi(\vec{r}) = \cos^{-1}(F(\vec{r}) - 1)$, where $F(\vec{r})$ is scaled to have a peak value of 2 and a minimum value of zero.

From this discussion, we can see that the intensity of the phase modulating light pulse should be proportional to the inverse cosine of the required lithographic pattern. This, in turn, implies that the intensities of the phase modulating light should be $I(\vec{r}) = I_0 \cos^{-1}(F(\vec{r}) - 1)$, where I_0 is a constant.

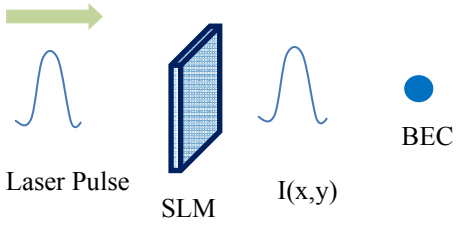

Figure 3. The proposed technique to imprint spatially varying phase pattern to a BEC. See text for details.

D. Lens system

In the previous section, it was shown that the phase modulation required to generate the lithographic pattern is performed using optical intensity variation. Light diffraction limits the resolution of this intensity variation to the scale of hundreds of nanometers. In our proposed atomic lithography system, we aim to achieve lithography in the single nanometer scale. Hence, an atomic lens system is required to shrink the wave packet to the desired scale after pattern phase imprinting. The lens system also plays a crucial role in suppressing wave packet distortion after phase imprinting. The phase imprinting step changes the momentum profile of the BEC order parameter. Free space propagation after this step will lead to distortion and loss of the lithographic pattern information. A lens system is required to perform imaging of the wave packet until the pattern is deposited on the substrate.

Previously [12], we developed a quantum mechanical wavefunction diffraction theory using linear Schrödinger equation and assuming the wavefunction of an atom to be two dimensional only. This theory was then used to develop an analytic transfer function for free space propagation, as well as for propagation through a lens realized via light shift. The transfer function was then used to design a Fourier transform system that consists of two lenses separated by some distance. Here, we first extend this model to the case where the spatial variation of the wavefunction along the direction of propagation is also taken into account. This model is used to produce the design for the lithographic system. However, since the GPE is nonlinear, the actual

behavior of the BEC order parameter is, obviously, expected to deviate from the ideal behavior. Numerical simulations of the evolution of the BEC order parameter were carried out. When discussing the results of these simulations, we will point out the extent to which the behavior of the BEC based system deviates from the linear diffraction theory.

To develop the transfer function of the free space propagation of a 3D wave function we start with the 3D Schrodinger equation

$$i\hbar\frac{\partial\Psi(\vec{r},t)}{\partial t}=-\frac{\hbar^2}{2m}\left(\frac{\partial^2}{\partial x^2}+\frac{\partial^2}{\partial y^2}+\frac{\partial^2}{\partial z^2}\right)\Psi(\vec{r},t) \qquad (8)$$

All solutions of this equations can be expressed as a linear superposition of the plane wave solution $A\exp(i\vec{k}.\vec{r}-i(\hbar/2m)|k|^2 t)$, where A is some constant. After a free space propagation of time T, the Fourier domain expression of the wavefunction can be expressed as

$$\Phi(\vec{k},T)=\int\Psi(\vec{r},T)e^{-i\vec{k}.\vec{r}}d\vec{r}=\int\Psi(\vec{r},0)e^{-i(\hbar/2m)|k|^2T}e^{-i\vec{k}.\vec{r}}d\vec{r}=\Phi(\vec{k},0)e^{-i(\hbar/2m)|k|^2T}. \qquad (9)$$

Hence, the transfer function for a free space propagation of time T is given by $H(\vec{k})=\exp(-i(\hbar/2m)|\vec{k}|^2T)$. The corresponding impulse response is $h(\vec{r})=(-im/2\pi\hbar T)^{3/2}\exp(im|\vec{r}|^2/2\hbar T)$. Consequently, for an arbitrary wavefunction $\Psi_{in}(\vec{r})$ at time $t=0$, the wavefunction expression at $t=T$ can be calculated via convolution to give

$$\Psi_{out}(\vec{r})=(-im/2\pi\hbar T)^{3/2}e^{im|\vec{r}|^2/2\hbar T}\int\Psi_{in}(\vec{r}')e^{i(m/2\hbar T)|\vec{r}'|^2}e^{-i(m/\hbar T)\vec{r}.\vec{r}'}d\vec{r}', \qquad (10)$$

which is analogous to the Fresnel diffraction integral from classical optics. Guided by this expression, a Fourier transform lens system can be achieved by using two instances of light shift induced phase modification separated by a free space propagation of time T_{lens}. The first phase shift modification process will add a phase of $-(m/2\hbar T_{lens})|\vec{r}|^2$ to the wavefunction $\Psi_{in}(\vec{r})$. After a free space propagation of time T_{lens}, the wavefunction is expressed as

$$\Psi(\vec{r})=(-im/2\pi\hbar T_{lens})^{3/2}e^{i(m/2\hbar T_{lens})|\vec{r}|^2}\int\Psi_{in}(\vec{r}')e^{-i(m/\hbar T_{lens})\vec{r}.\vec{r}'}d\vec{r}'. \qquad (11)$$

We design the second phase modification to add a phase of $-(m/2\hbar T_{lens})|\vec{r}|^2+3\pi/4$. The resulting wavefunction is $\Psi(\vec{r})=(m/2\pi\hbar T_{lens})^{3/2}\int\Psi_{in}(\vec{r}')e^{-i(m/\hbar T_{lens})\vec{r}.\vec{r}'}d\vec{r}'$.

This analysis shows that the resulting wavefunction after the lens system is a scaled Fourier Transform (FT) of the input wavefunction

$$|\Psi_{out}(\vec{r})\rangle=\left(\frac{m}{2\pi\hbar T_{lens}}\right)^{3/2}\left|\Phi_{in}\left(\frac{m}{\hbar T_{lens}}\vec{r}\right)\right\rangle. \qquad (12)$$

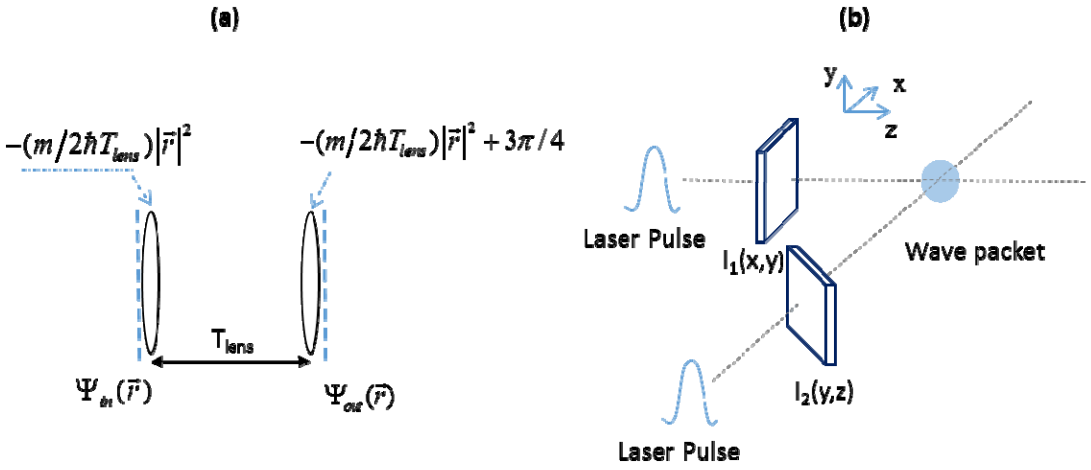

Figure 4. a) Fourier Transform atomic lens scheme b) proposed implementation to create three-dimensional phase shift. See text for details.

This concept of creating a FT lens pair is illustrated schematically in Figure 4(a). In Figure 4(b) we illustrate the fact that light pulses applied in orthogonal direction are necessary in order to ensure the FT process occurs in all three dimensions. One of these pulses is launched in the positive Z direction along the direction of motion of the wave packet. The other is launched in the positive X direction. Each of the two pulses go through a spatial light modulator (SLM) to produce two-dimensional intensity variation in the plane normal to the pulse direction. For instance, to generate the light shift corresponding to the first of the two FT lenses, each point (x, y, z) of the wave packet should have an additional phase shift of $-(m/2\hbar T_{lens})\left(x^2+y^2+z^2\right)$. To create this phase shift, the SLM for the pulse moving in the Z direction can be used to modify the pulse intensity in the x-y plane by $I_1(x,y)=I_{10}(x^2+0.5y^2)$ which add a phase shift of $\alpha_1(x^2+0.5y^2)$, where $\alpha_1 \propto (I_{10}/4\delta)\tau$, as discussed earlier. Similarly, the SLM for the pulse moving in the x direction can be used to add a phase shift of $\alpha_2(z^2+0.5y^2)$. Engineering α_1 and α_2 to be both equal to $-(m/2\hbar T_{lens})$ will result in the required phase shift of $-(m/2\hbar T_{lens})\left(x^2+y^2+z^2\right)$. The timing of the pulses is controlled such that they intersect at the position of the wave packet, hence generating the required three-dimensional intensity variation.

It is obvious from the derivation shown above that the nonlinearity of the GPE would cause significant deviation in the behavior of the order parameter as it moves through free space and lenses. The model we just derived is, therefore, only used as a guideline for designing the system. The actual behavior of the system will be determined via numerical simulation which takes into account the nonlinearity of the GPE.

In Figure 5, we show an expanded version of the lithography system, now including lenses used for demagnification. Following the imprinting of the pattern phase, indicated as Φ_p in the upper leg of the AI, we apply two successive FT lens pairs, indicated by Φ_1 and Φ_2 for the first pair, and Φ_3 and Φ_4 for the second pair. It follows from equation (12) that the wavefunction after Φ_4 is a scaled down version of the wavefunction before Φ_1 by a factor T_b/T_a ($T_b<T_a$), where T_a (T_b) is

the time difference between Φ_1 and Φ_2 (Φ_3 and Φ_4). For the lower arm of the AI, a lens system identical to the one used for the upper arm is used.

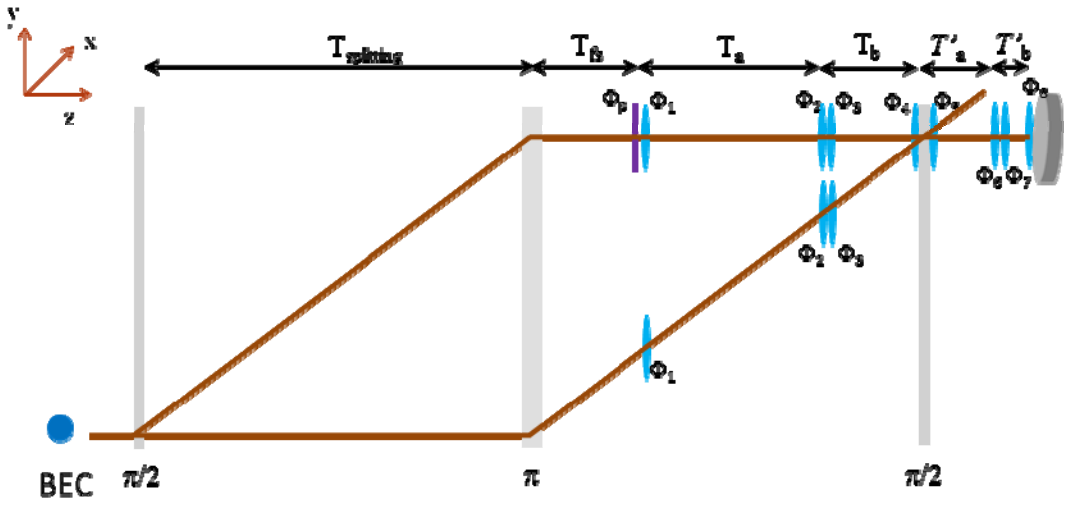

Figure 5. Atom lithography system with the implementation of the lenses shown explicitly. Φ_p is the pattern phase shift. See text for details.

The last π/2 pulse causes the two arms of the AI to interfere. The output after this pulse is split into two components. The component parallel to the Z direction is used for lithography. Since the substrate on which the pattern is to be deposited cannot be placed at the location right after this π/2 pulse, it is necessary to employ two more FT lens pairs, indicated by Φ_5 and Φ_6 for the first pair, and Φ_7 and Φ_8 for the second pair. Note that the final pattern on the substrate will be a scaled version of the pattern produced immediately after the last π/2 pulse, the scale factor being T_b'/T_a'.

The shown phase shifts in Figure 5 are given by: $\Phi_1 = -m|\vec{r}|^2/2\hbar T_a$, $\Phi_2 = -m|\vec{r}|^2/2\hbar T_a + 3\pi/4$, $\Phi_3 = -m|\vec{r}|^2/2\hbar T_b$, $\Phi_4 = -m|\vec{r}|^2/2\hbar T_b - 3\pi/4$, $\Phi_5 = -m|\vec{r}|^2/2\hbar T_a'$, $\Phi_6 = -m|\vec{r}|^2/2\hbar T_a' + \frac{3\pi}{4}$, $\Phi_7 = -m|\vec{r}|^2/2\hbar T_b'$, $\Phi_8 = -m|\vec{r}|^2/2\hbar T_b' + \frac{3\pi}{4}$. To ensure symmetric operation of the AI, the time separation between the three pulses of the AI should be equal. Hence, $T_{splitting} = T_{fs} + T_a + T_b$.

The used lens system in figure 5 can be further simplified to make it more practical. The basis of this simplification is to combine consecutive light shift processes like Φ_2 and Φ_3 into a single process. This is simply done by adding the phase variation of the two processes. Consequently, the intensity variation of the combined process is the addition of the intensity variation of the individual components. To get further simplification, the lens system can be rearranged to increase the number of consecutive light shift processes, for example, by replacing the phase modification process Φ_4 by a new phase modification process Φ_x that occurs after Φ_1. This replacement will allow combining of Φ_1 and Φ_x into a single phase modification process. Figure 6 illustrates the simplification procedure where the original arrangement is shown in set (a), the rearranged system is shown in set (b), and finally the simplified system is shown in set (c).

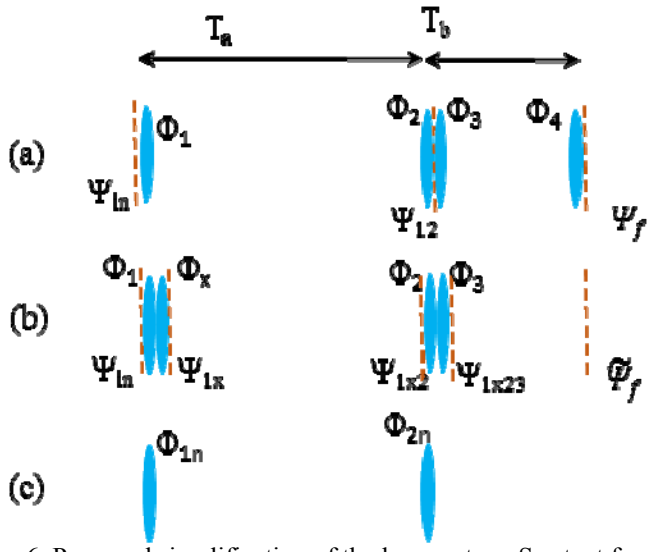

Figure 6. Proposed simplification of the lens system. See text for details.

The phase Φ_x is assumed to take the form $\Phi_x = -m|\vec{r}|^2/2\hbar T_x|\vec{r}|^2 + \phi_x$ where T_x and ϕ_x are determined by the requirement that the response of the rearranged system be the same as the original system. For set (a) in Figure 6, assuming the wavefunction before Φ_1 is expressed as $\Psi_{in}(\vec{r})$ and using Equation (12), the wavefunction just after Φ_2 is given by:

$$\Psi_{12}(\vec{r}) = (m/2\pi\hbar T_a)^{3/2}\int \Psi_{in}(\vec{r}\,')e^{-i(m/\hbar T_a)\vec{r}.\vec{r}'}d\vec{r}\,'. \qquad (13)$$

Similarly, after Φ_4 the wavefunction is given by:

$$\begin{aligned}
\Psi_f(\vec{r}) &= (m/2\pi\hbar T_b)^{3/2}\int \Psi_{12}(\vec{r}\,'')e^{-i(m/\hbar T_b)\vec{r}.\vec{r}''}d\vec{r}\,'' \\
&= (m/2\pi\hbar T_b)^{3/2}\int\left[(m/2\pi\hbar T_a)^{3/2}\int \Psi_{in}(\vec{r}\,')e^{-i(m/\hbar T_a)\vec{r}''.\vec{r}'}d\vec{r}\,'\right]e^{-i(m/\hbar T_b)\vec{r}.\vec{r}''}d\vec{r}\,'' \\
&= \left(m^2/(2\pi\hbar)^2 T_a T_b\right)^{3/2}\int\left[\int e^{-i(m/\hbar)\vec{r}''.(\vec{r}'/T_a+\vec{r}/T_b)}d\vec{r}\,''\right]\Psi_{in}(\vec{r}\,')d\vec{r}\,' \qquad (14) \\
&= \left(m^2/(2\pi\hbar)^2 T_a T_b\right)^{3/2}\int\left[(2\pi\hbar/-im)\,\delta(\vec{r}\,'/T_a+\vec{r}/T_b)\right]\Psi_{in}(\vec{r}\,')d\vec{r}\,' \\
&= -i\,(m/2\pi\hbar)^2\left(1/T_a T_b^3\right)^{1/2}\Psi_{in}(-\vec{r}T_a/T_b)
\end{aligned}$$

For set (b) in Figure 6, assuming the wavefunction before Φ_1 is $\Psi_{in}(\vec{r})$, the wavefunction just after Φ_x is given by:

$$\Psi_{1x}(\vec{r}) = \Psi_{in}(\vec{r})\exp\left(-im|\vec{r}|^2/2\hbar T_a\right)\exp\left(-im|\vec{r}|^2/2\hbar T_x + i\phi_x\right). \qquad (15)$$

Using Equation (10), the wavefunction just before Φ_2 can be expressed as:

$$\Psi_{1x2}(\vec{r}) = (-im/2\pi\hbar T_a)^{3/2}e^{i(m/2\hbar T_a)|\vec{r}|^2+i\varphi_x}\int \Psi_{in}(\vec{r}\,')e^{-i(m/2\hbar T_x)|\vec{r}\,'|^2}e^{-i(m/\hbar T_a)\vec{r}.\vec{r}'}d\vec{r}\,'. \qquad (16)$$

Therefore, after Φ_3 the wave function is given by:

$$\Psi_{1x23}(\vec{r}) = (m/2\pi\hbar T_a)^{3/2}e^{-i(m/2\hbar T_b)|\vec{r}|^2+i\varphi_x}\int \Psi_{in}(\vec{r}\,')e^{-i(m/2\hbar T_x)|\vec{r}\,'|^2}e^{-i(m/\hbar T_a)\vec{r}.\vec{r}'}d\vec{r}\,' \qquad (17)$$

After free space propagation of time T_b the wavefunction is given by:

$$
\begin{aligned}
\tilde{\Psi}_f(\vec{r}) &= (-im/2\pi\hbar T_b)^{3/2} e^{i(m/2\hbar T_b)|\vec{r}|^2 + i\varphi_x} \int \Psi_{1x\,23}(\vec{r}\,'') e^{i(m/2\hbar T_b)|\vec{r}\,''|^2} e^{-i(m/\hbar T_b)\vec{r}.\vec{r}\,''} d\vec{r}\,'' \\
&= (-im^2/(2\pi\hbar)^2 T_a T_b)^{3/2} e^{i(m/2\hbar T_b)|\vec{r}|^2 + i\varphi_x} \int\int \Psi_{in}(\vec{r}\,') e^{i(m/2\hbar T_x)|\vec{r}\,'|^2} e^{-i(m/\hbar T_a)\vec{r}\,''.\vec{r}\,'} d\vec{r}\,' e^{-i(m/\hbar T_b)\vec{r}.\vec{r}\,''} d\vec{r}\,'' \\
&= (-im^2/(2\pi\hbar)^2 T_a T_b)^{3/2} e^{i(m/2\hbar T_b)|\vec{r}|^2 + i\varphi_x} \int \left[\int e^{-i(m/\hbar)\vec{r}\,''.(\vec{r}\,'/T_a + \vec{r}/T_b)} d\vec{r}\,'' \right] \Psi_{in}(\vec{r}\,') e^{i(m/2\hbar T_x)|\vec{r}\,'|^2} d\vec{r}\,' \qquad (18) \\
&= (-im^2/(2\pi\hbar)^2 T_a T_b)^{3/2} e^{i(m/2\hbar T_b)|\vec{r}|^2 + i\varphi_x} \int \left[(2\pi\hbar/-im)\,\delta(\vec{r}\,'/T_a + \vec{r}/T_b) \right] \Psi_{in}(\vec{r}\,') e^{i(m/2\hbar T_x)|\vec{r}\,'|^2} d\vec{r}\,' \\
&= (-i)^{1/2} (m/2\pi\hbar)^2 (1/T_a T_b^3)^{1/2} \Psi_{in}(-\vec{r}T_a/T_b) e^{im|\vec{r}|^2 (1/T_b - T_a^2/T_x T_b^2)/2\hbar + i\varphi_x}
\end{aligned}
$$

By choosing T_x to have the form $T_x = T_a^2/T_b$ and setting $\phi_x = -\pi/4$, we see that $\tilde{\Psi}_f(\vec{r}) = \Psi_f(\vec{r})$, so that set (b) is equivalent to set (a). Finally, set (c) is the result of combining consecutive phase modification processes such that $\Phi_{1n} = \Phi_1 + \Phi_x$ and $\Phi_{2n} = \Phi_2 + \Phi_3$.

The same simplification procedure can be applied to the lens system used after the last $\pi/2$ pulse of the AI by replacing the phase Φ_8 by a phase $\Phi_{x'}$ that occurs directly after Φ_5. By a similar derivation $\Phi_{x'}$ takes the form $\Phi_{x'} = -m|\vec{r}|^2/2\hbar T_{x'}|\vec{r}|^2 + \pi/4$, where $T_{x'} = T_{a'}^2/T_{b'}$. Simplifying the structure by combining consecutive phase modification processes creates $\Phi_{3n} = \Phi_5 + \Phi_{x'}$ and $\Phi_{4n} = \Phi_6 + \Phi_7$. Figure 7 shows the simplified version of the atom lithography system. In the simplified system, the pattern phase modification process is combined with the phase modification process Φ_{1n} to create a phase $\Phi_{1p} = \Phi_p + \Phi_{1n}$.

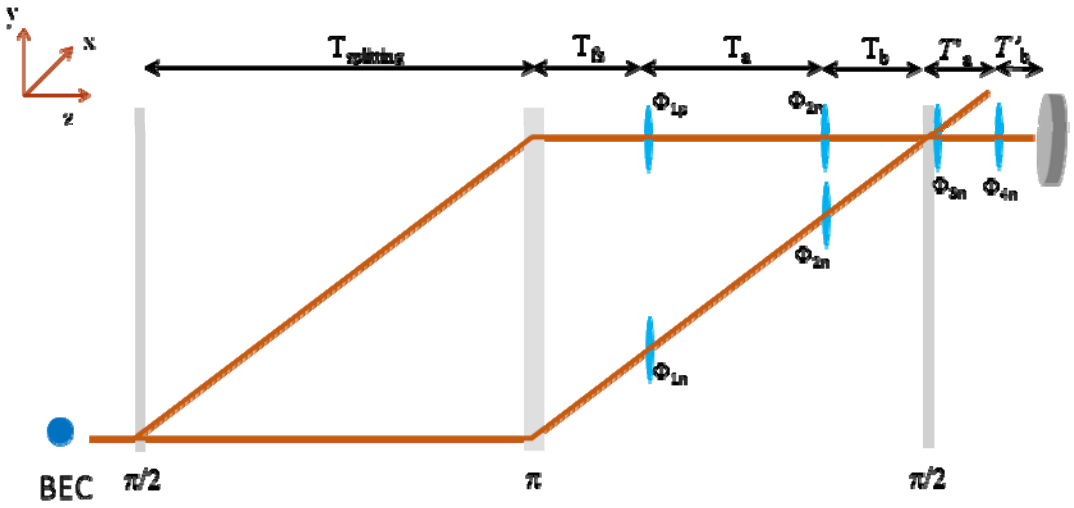

Figure 7. Simplified atom lithography system. See text for details.

IV. Practical Considerations

For possible practical implementation of this lithography system, we propose the use of ^{87}Rb BEC. Consider first the excitations process for the AI, which can be implemented using the D1 line transitions [26]. The Raman transition consists of states $|1\rangle \equiv 5^2S_{1/2}$ (F=1, m_F=1), $|2\rangle \equiv 5^2P_{1/2}$ (F'= 2, m_F= 0) and $|3\rangle \equiv 5^2S_{1/2}$ with (F= 2, m_F= -1), with the quantization axis chosen to be in the $\hat{y}$ direction. These levels are shown in Figure 8.a. The energy difference between states

$|1\rangle$ and $|3\rangle$ is $\omega_{13} = 2\pi \times 6.8 \times 10^9$ s^{-1}. The $|1\rangle \leftrightarrow |2\rangle$ and $|2\rangle \leftrightarrow |3\rangle$ transitions are excited by applying σ^- and σ^+ polarized fields, respectively. Here, we assume the detuning and the Rabi frequencies - denoted as δ and Ω, respectively - to be the same for both Raman transitions. In order to suppress the effect of spontaneous emission, we have to satisfy the condition

$$(\Omega/\delta)^2 \Gamma \tau << 1, \qquad (19)$$

for all transitions, where τ is the interaction time and $\Gamma = 3.61 \times 10^7$ s^{-1} is the decay rate of $|2\rangle$. We also need to ensure that, for example, the σ^+ polarized field for the $|2\rangle \leftrightarrow |3\rangle$ transition does not produce a significant transition between the $|1\rangle$ and $|3\rangle$ states. This requires that $\delta << \omega_{13}$. Hence, we choose $\delta = \omega_{13}/10 = 118.35\ \Gamma$. For the Raman interaction pulses, the longest interaction is required for the π pulse. For that interaction, $\Omega_R \tau = \pi$ should be satisfied, where $\Omega_R = \Omega^2/2\delta$ is the Raman Rabi frequency. Setting the longest interaction time to be $\tau = 1\mu s = 36.1\ \Gamma^{-1}$ s, the Rabi frequency is $\Omega = 4.54\ \Gamma$ which satisfies Equation (19). The value of Ω for each transition is related to the intensity I of the beam applied to this transition by the relation $\Omega^2 = (I/I_{sat})\Gamma^2/2$, where I_{sat} is the saturation intensity. For the $|3\rangle \leftrightarrow |2\rangle$ transition the saturation intensity is $I_{sat} = 3.34$ mW/cm^2 and for the $|1\rangle \leftrightarrow |2\rangle$ transition $I_{sat} = 3*3.34$ mW/cm^2 [26]. Hence, in order to have the same Rabi frequency for both transitions, the intensity of the field applied to the $|1\rangle \leftrightarrow |2\rangle$ transition has to be a factor of 3 larger than the intensity of the field applied to the $|3\rangle \leftrightarrow |2\rangle$ transition. Consequently, for $\Omega = 4.54\ \Gamma$, the required intensities are $I = 137.7$ mW/cm^2 for the $|3\rangle \leftrightarrow |2\rangle$ transition and $I = 413.1$ mW/cm^2 for the $|1\rangle \leftrightarrow |2\rangle$ transition.

Consider next the process for producing the AC-Stark shift needed for the phase mask as well as the lenses. As we have described earlier, the beams used for producing these shifts will propagate in the $\hat{x}$ and the $\hat{z}$ directions, both being perpendicular to the quantization direction, $\hat{y}$, chosen to be parallel to the direction of propagation of the AI beams. Thus, the AC-stark shift fields must be π-polarized. For the upper arm, we can use the π-transition coupling state $|1\rangle$ to the F'=2, m_F =1 excited state. The saturation intensity for this transition is $I_{sat} = 3.34$ mW/cm^2. For the lower arm, we can use the π-transition coupling state $|3\rangle$ to the F'=2, m_f = -1 excited state. The saturation intensity for this transition is $I_{sat} = 3*3.34$ mW/cm^2. These transitions are illustrated in Figure 8.b. As discussed earlier, the phase shift produced for a given combination of Rabi frequency, detuning and interaction time is given by $(\Omega^2/4\delta)\tau$. Since any phase shift is equivalent to any other phase shift differing by integer multiples of 2π, the maximum useful value of the Rabi frequency for a given detuning and interaction time is given by $(\Omega_{max}^2/4\delta)\tau = 2\pi$. As an example, we consider the case where the value of δ for each of the AC-Stark shift fields is the same as that employed for the AI beams. This is an experimentally convenient choice, allowing the beams to be generated from the same laser used for producing the AI. Furthermore, it ensures that the effect of the π-polarized field used for one AI leg has minimal effect on the π-transition for the other leg. In order to suppress the effect of spontaneous emissions, we must also satisfy Equation (19) for these beams. Keeping this in mind, we choose

the values of Ω_{max} to be the same as the values used for the AI (i.e., $\Omega_{max} = 4.54\ \Gamma$). The corresponding value of τ is then found to be $\tau = 4\mu s$.

It is easy to verify that Equation (19) is satisfied for this combination of parameters. Finally, For the saturation intensities noted above for the π-transitions, producing a value of $\Omega_{max} = 4.54\ \Gamma$ requires the intensity for the upper leg of to be $I = 137.7\ \mathrm{mW/cm^2}$ and that for the lower leg to be $I = 413.1\ \mathrm{mW/cm^2}$.

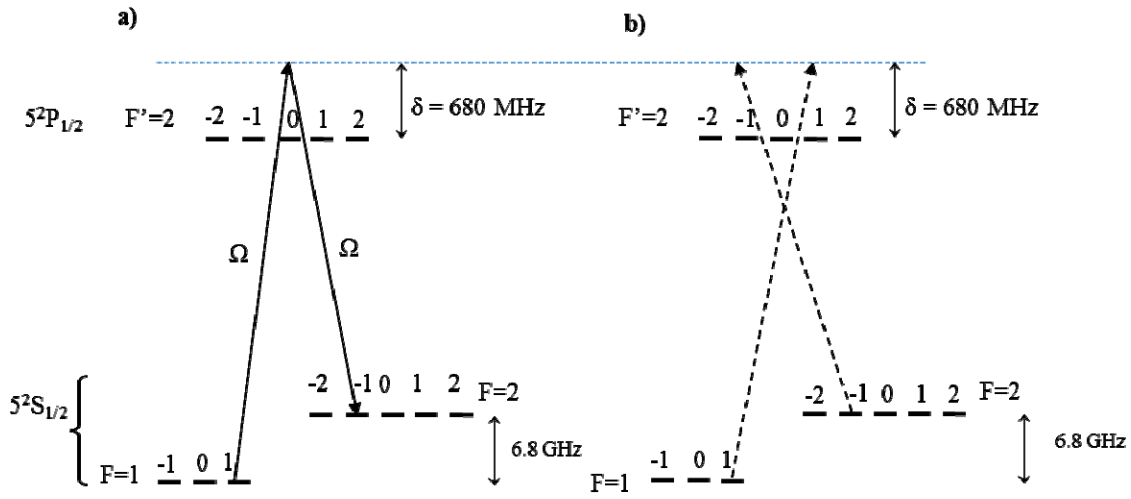

Figure 8. Laser interactions required for the proposed atom lithography system. a) Laser interactions required for the Raman AI (Solid lines). b) AC-stark interactions required to implement the lens system for both AI arms (Dashed lines). See text for details.

Another practical consideration is the effect of gravity, and resulting constraints on the physical dimension of the AI. A terrestrial implementation of the system can be realized by choosing the z-axis to be the downward vertical direction, and releasing the BEC downward under the effect of gravity. In this case, using a separation time of 1 second between the AI Raman pulses will require a height of ~ 10 meters. However, such a long separation time is not necessary in practice. The minimum value of the separation time is dictated by the need to ensure clear separation between the spatial extents of the BEC order parameters in the two arms of the AI. For the simulations we have reported here, the width of the order parameter at the onset of the AI process is 0.1 mm (full width at half maximum). The recoil velocity of ^{87}Rb for the D1 transition being ~ 0.6 cm/sec, a clear spatial separation can be achieved for a separation time of ~50 msec. In order to accommodate the optical pulses that act as the lens system, a greater separation is useful. Use of a separation time of ~100 msec would satisfy this requirement. For this choice, the height required for the AI would be ~10 cm. It should also be noted that the trajectories of the split components will not be linear. However, the ballistic trajectories will not affect the behavior of the lithographic system if the time separation between the first π/2 pulse and the π pulse is the same as that between the π pulse and the second π/2 pulse.

V. Numerical Simulations

In numerical simulations, BEC order parameters are represented by three dimensional finite grids. The grid limit in each direction was chosen to be large enough such that the order parameter values at the edges of the grid are negligible. The grid resolution is selected to guarantee both the convergence of the numerical algorithms and the ability to show the fine details of the simulated lithographic patterns. To handle the computational complexity, parallel computing was used by utilizing the concept of domain decomposition. All simulations were performed in the spatial domain in order to include the effect of the nonlinear term of in the GPE equation.

As discussed in section III, the initial condition of the BEC order parameter was taken to be in the ground state $|1\rangle$ with Gaussian profiles in all directions, as described in Equation (3). The Gaussian profile width is taken to be equal in each direction: $\delta_x = \delta_y = \delta_z$. A typical practical value of this width is 30 μm [18, 27]. The other parameters of the GPE equations correspond to a condensate ^{87}Rb [26]. For the AI, we assume that the time delay between the first π/2 pulse and the π pulse is the same as that between the π pulse and the second π/2 pulse. We take this time to be 1 second, which is enough to ensure complete spatial separation of the different BEC components. Free space propagation anywhere in the system is simulated using the GPE with the finite difference approximations of Equation (6) while setting the external potential term to zero. Atom-light interaction is simulated using Equation (7) under the same finite difference approximations.

The atom lithography system can be used without the lens system when scaling of the pattern is not needed. In this case, the pattern phase imprinting should occur immediately before the last π/2 pulse to avoid distortion of the pattern. Figure 9 shows a three-dimensional image of the interference result using a pattern that has the shape of a plus sign.

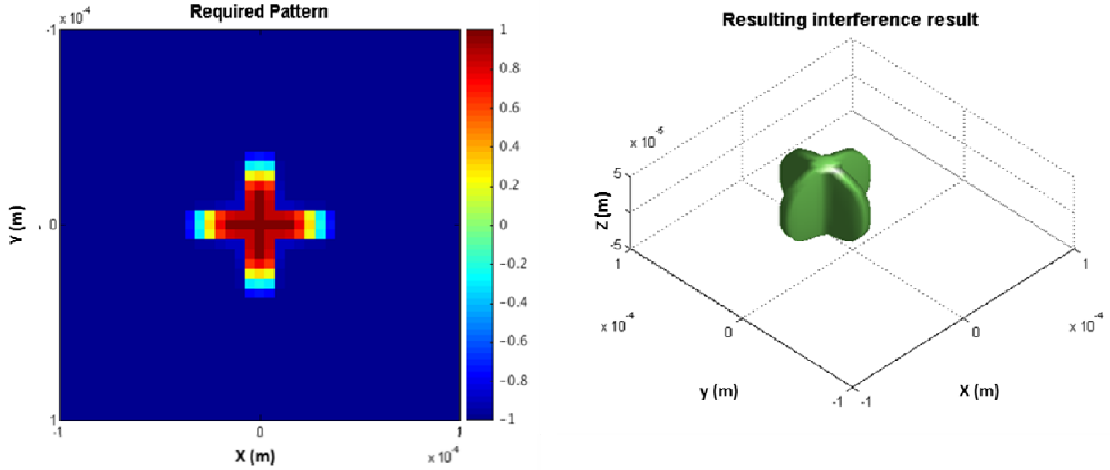

Figure 9. a) The required lithographic pattern b) the resulting distribution of the order parameter after the atomic interferometer.

For producing scaled versions of the pattern, it is necessary to use the lens system. We recall that the lens system derived in section III.D is based on the Schrödinger equations (SE) for a single

atom. In contrast, the evolution of the BEC order parameter follows the nonlinear GPE. As such, the input-output relation for the lens system, when applied to the BEC order parameter, is expected to deviate to some extent from the ideal result stated in section III.D. We first compare the behavior of a single atom with the performance of BEC wave packets for different number of atoms. This comparison will prove useful in determining the constraints under which the proposed lens system can be used for BEC wave packets. Specifically, we start with a system that has a Gaussian distribution of probability in X, Y and Z directions. We then study the evolution of this distribution under several different scenarios. First, we treat the system as the wavepacket of a single atom. In this case, we use SE to determine the amplitude distribution of the wavefunction after evolution for a characteristic time scale. We choose this time scale to be 1 second since that is the duration of the dark zone in our scheme. Next, we use the same distribution for the BEC order parameter of a condensate of N atoms, and determine the amplitude distribution of the order parameter after evolution for the same characteristic time. We consider three different values of N: 10^3, 10^4 and 10^5. These results are illustrated in Figure 10. As can be seen from these results, the deviation from the single atom case increases with increasing values of N. This is consistent with the fact that, for a given volume, the importance of the nonlinear term of the GPE increases with N. The simulation results also agree with the experimental results of [18, 28], which shows that a BEC with a large number of atoms undergo a significant size expansion due to the interaction of atoms in the BEC.

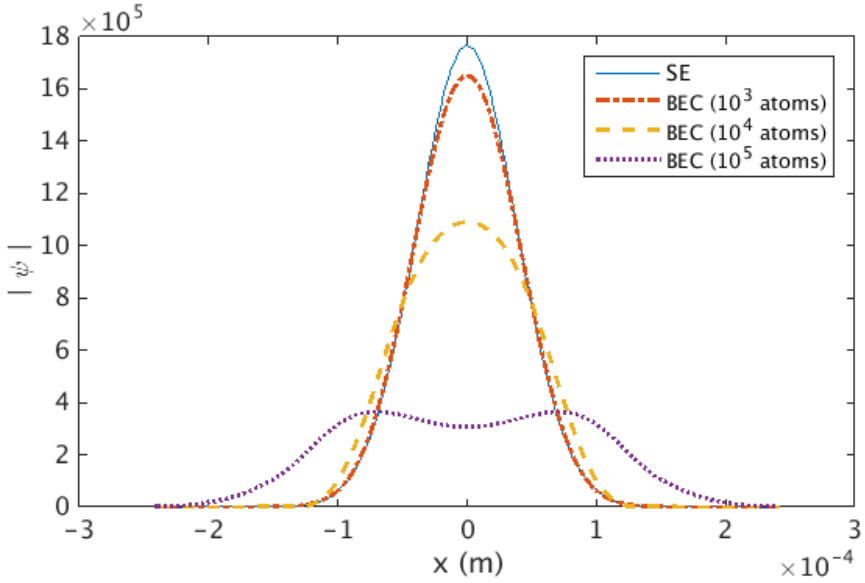

Figure 10. Comparison between the x cross section of the single atom wavefunction and the BEC order parameter after a free space propagation of 1 second.

From Figure 10, it is reasonable to assume that the behavior of a BEC with $N=10^3$ is close to that of a single atom. For the parameters considered here, this corresponds to a density of $1\times10^{10}cm^{-3}$. According to [27], such a low density can be achieved by adiabatically cooling the condensate. A different scenario for achieving a single atom behavior is to use a BEC with a higher number of atoms (higher density) while reducing the condensate scattering length a_s. According to the GPE equation, an order of magnitude reduction of the scattering length a_s allows for an order of magnitude increase in N while keeping the nonlinear term unchanged. The scattering length of a ^{87}Rb BEC can be controlled by using Feshbach resonance [29]. In our simulations, we choose to use the parameters of ^{87}Rb BEC with 1000 atoms for the naturally occurring value of a_s.

Figure 11 shows the performance of the original and rearranged lens systems on a BEC wave packet of the selected parameters. The figure shows that for both lens configurations, the BEC wave packet after the lens system is almost identical to that before the lens system when Ta = Tb. We get a demagnification ratio of two when Ta = 2Tb. These numerical results show that selecting the parameters of the BEC wave packet to be within the proper constraints allows the use of the lens system that was designed using Schrodinger equation without a significant loss of performance.

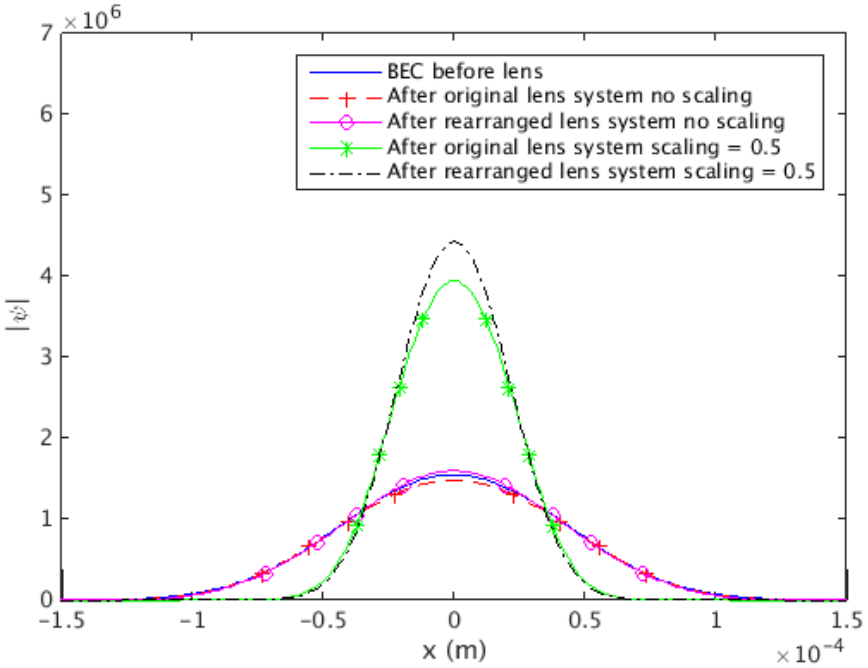

Figure 11. Cross section of the BEC order parameter after different configurations of the lens system.

In the rest of this section, we show the simulation results of the BEC lithography system. In order to evaluate the effect of the propagating BEC interference result on the substrate, the probability distribution of the order parameter is integrated over the propagation direction to calculate the equivalent two-dimensional effect. To test the properties of the lithography system, multiple patterns have been used, ranging from intersecting straight lines to circles. In these simulations, both the original lens arrangement and the modified lens arrangement were tested in order to establish that lens rearrangement does not affect the functionality of the system significantly. Figure 12 shows the result of the lithography system for a pattern that takes the shape of a plus sign using the rearranged and simplified lens system illustrated in Figure 7. The interference results are shown for three different cases: when no scaling is used, scaling with a ratio of 0.8 and scaling with a ratio of 2/3. Figure 13 shows the results for the same pattern using the original arrangement of the lens system illustrated in Figure 5. The case without pattern scaling is shown Figure 13.a , while Figure 13.b shows the result when a scaling ration of 0.8 is used. Comparison of these results shows that the two proposed lens systems are essentially equivalent. Figure 14 shows the lithography system results for a circular pattern with a radius of 30 μm using the original lens arrangement for the no scaling and 0.8 scaling scenarios. Figure 15 shows the results for the same circular pattern using the modified lens systems and using two

different scaling ratios. Figure 16 shows the simulations results using a letter n pattern for different scaling ratios. This figure illustrates the fact that the output is a mirrored version of the used pattern.

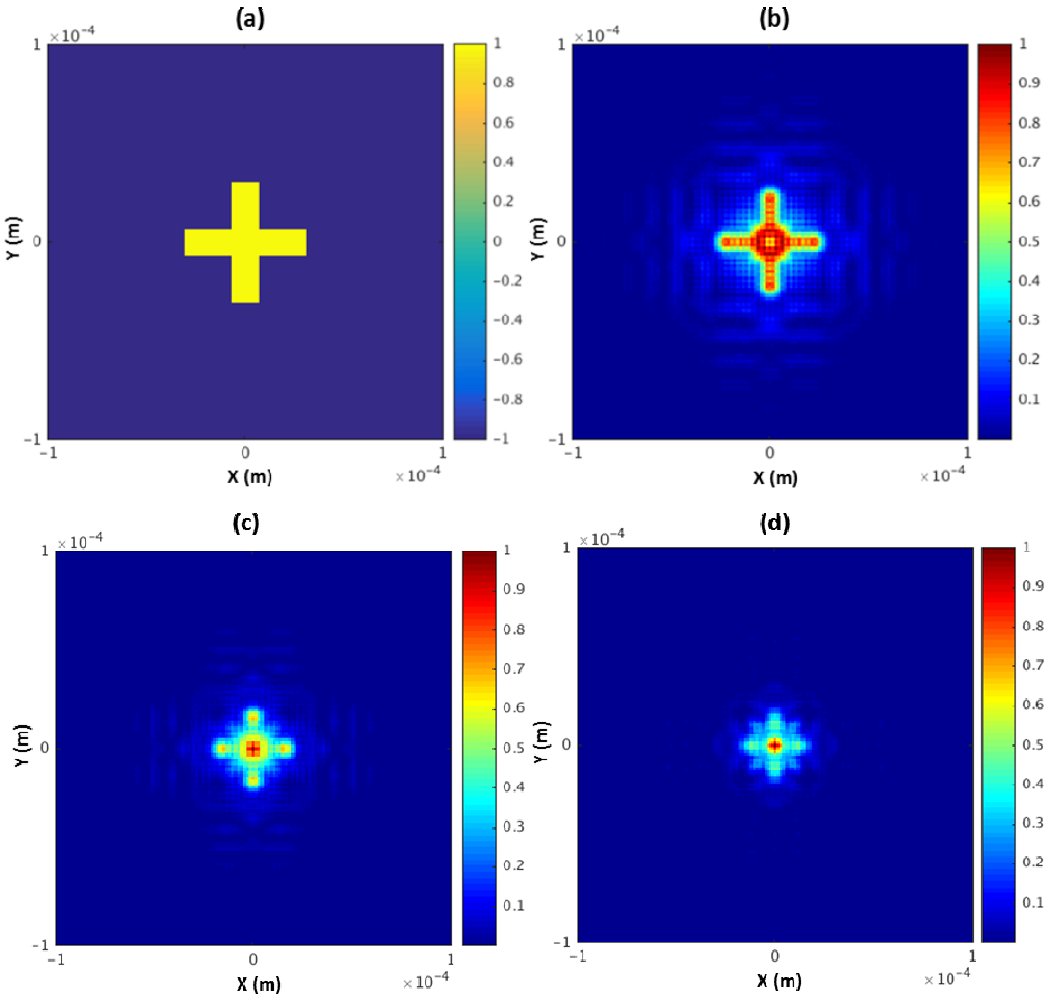

Figure 12. Result of the lithography system using the simplified lens configuration a) required lithographic pattern b) Normalized effective 2D probability distribution for unity scaling, c) for a scaling ratio of 0.8 d) for a scaling ratio of 2/3.

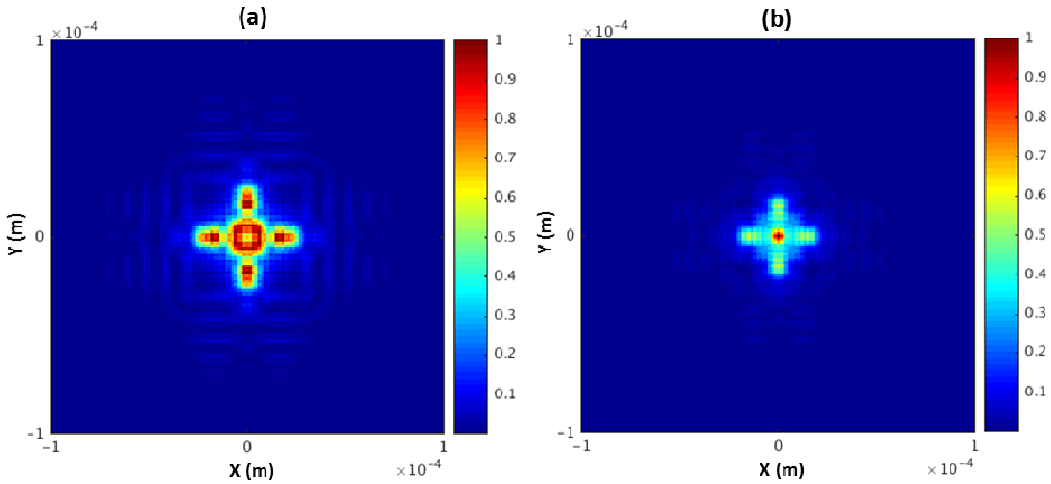

Figure 13. Normalized effective 2D probability distribution for a plus sign pattern using the original lens system a) with unity scaling b) with a scaling ratio of 0.8

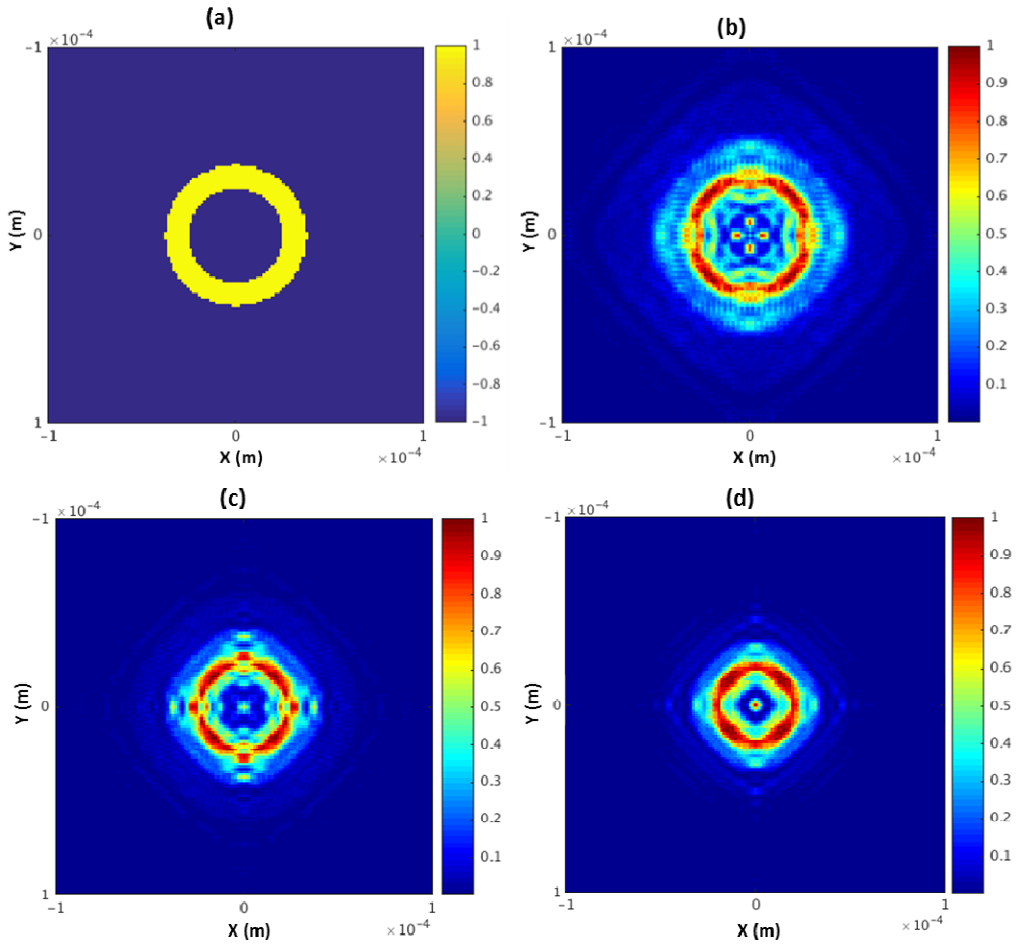

Figure 14. Results of the lithography system for a circular pattern using the simplified lens system a) the desired circular pattern b) Normalized effective 2D probability distribution for the unity scaling case. c) Result for a scaling ratio of 0.8 d) Result for a scaling ratio of 2/3

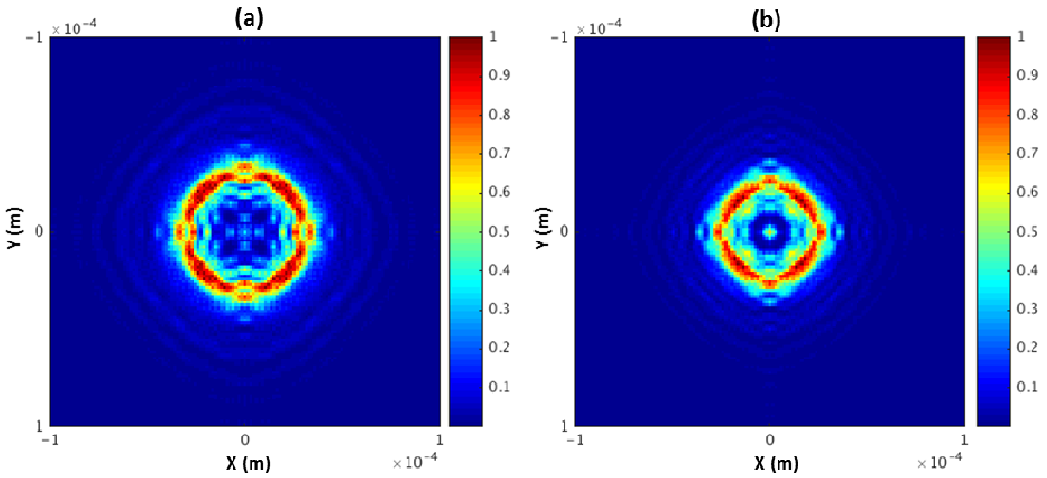

Figure 15. Results of the lithography system for a circular pattern using the original lens arrangement a) Normalized effective 2D probability distribution for unity scaling b) for a scaling ratio of 0.8.

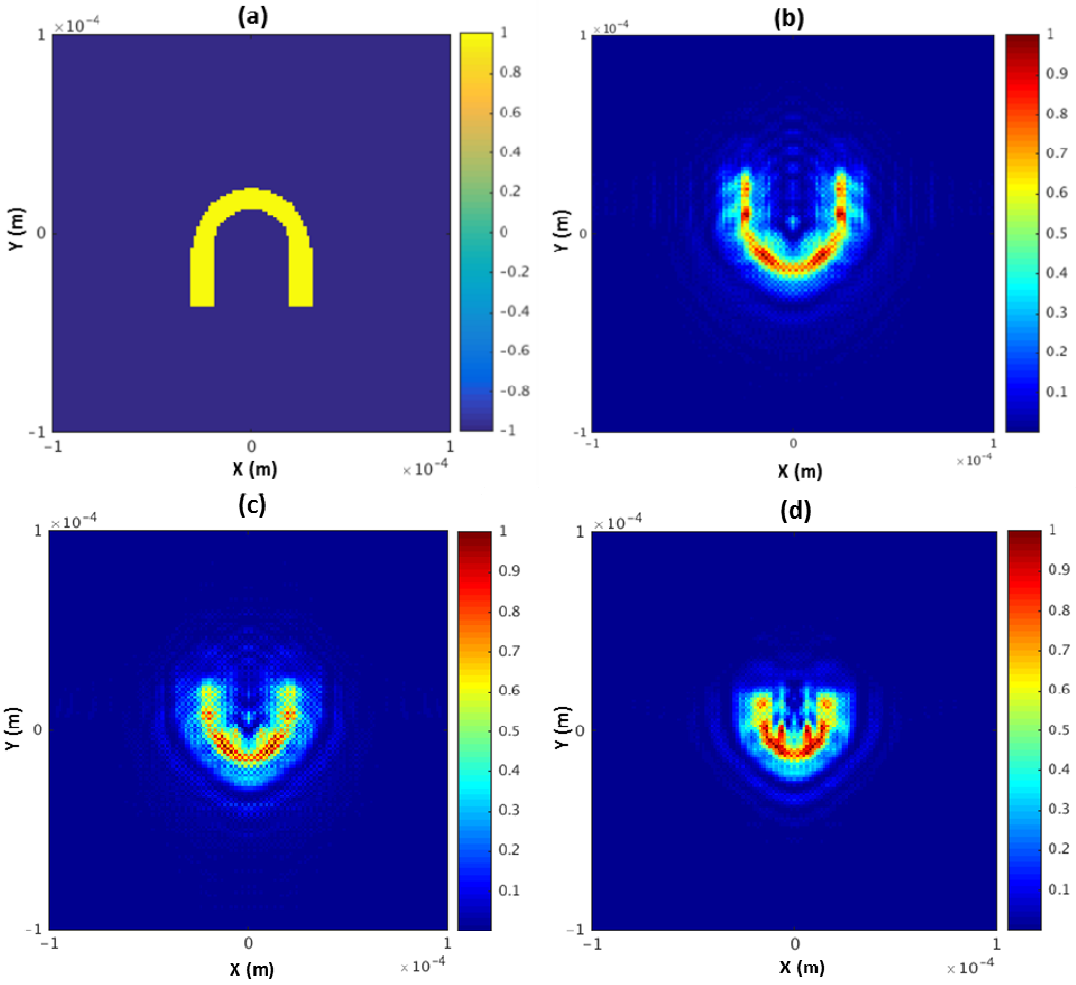

Figure 16. Results of the lithography system for a letter n pattern using the modified lens arrangement a) The desired letter n pattern b) Normalized effective 2D probability distribution for the unity scaling case c) Result with a scaling ratio of 0.8 d) Result with a scaling ratio of 2/3.

The simulation results indicate that the system can be used for arbitrary patterns. However, as can be seen in the previous figures, the interference results have some distortion. These errors result from limited spatial grid resolution. This explains why the distortion is larger for smaller lithographic patterns or when using a large scaling ratio like the case in Figure 16.d. These errors can be improved by using a finer spatial grid resolution. However, using a finer resolution will increase the computational complexity in a cubic manner because of the use of three-dimensional grids. The current simulations were performed using a custom developed explicit finite difference code running on Matlab. Using domain composition, it was possible to perform parallel processing on four cores of (Intel E5-2680) processor. Increasing the number of cores beyond four did not yield significant advantage because of the involved communication overhead between cores. Using a spatial resolution step of 0.05σ -where σ=30 μm is the standard deviation of the initial order parameter Gaussian distribution- the time required for the simulation of the whole AI system is about two weeks. Using a smaller spatial resolution would result in larger spatial grids and require much smaller simulation time steps leading to a much longer simulation time. In order to illustrate the effect of spatial resolution, in Figure 17 we compare the simulation results for the circular pattern shown in Figure 14.a using two different spatial resolutions. It is clear that when a larger resolution is used, larger simulation errors and distortion occurs.

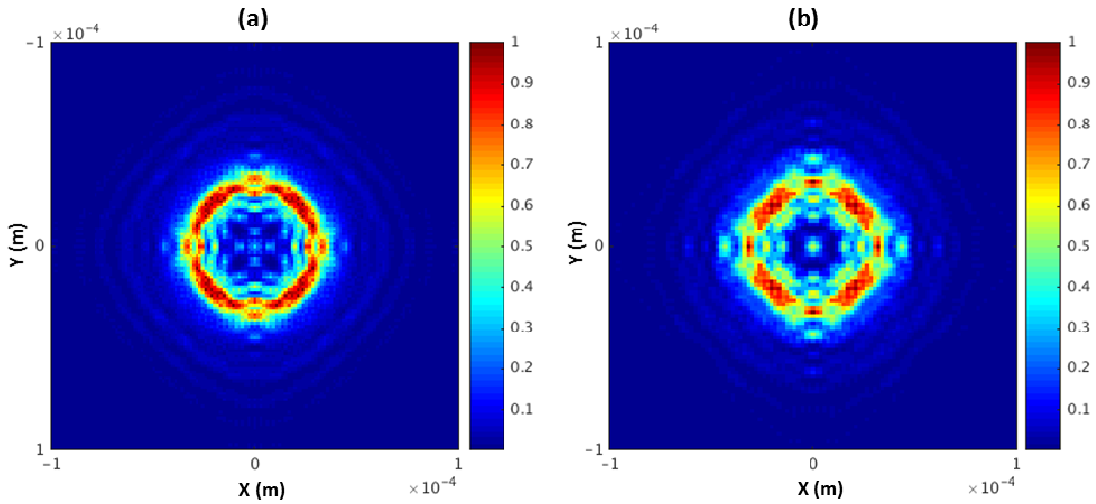

Figure 17. Results of the lithography system for a circular pattern for two different numerical simulation resolutions a) the spatial step size = 0.05σ b) the spatial step size = 0.0625σ, where σ is the standard deviation of the initial order parameter Gaussian distribution.

VI. Summary and Conclusion

In this paper, we have proposed an arbitrary pattern lithography system using the interference of BEC. A symmetric three pulse Raman atom interferometer (AI) is used to implement the system. The lithographic pattern is represented by a two-dimensional intensity variation, and is transformed into a two-dimensional phase variation in the BEC order parameter via the use of AC-stark shift induced by a pulsed laser field applied in one of the AI arms. The BEC probability distribution of the interference result at the end of the AI is proportional to the required pattern. In order to produce features smaller than the diffraction limit for the used optical system, we employ a three-dimensional atomic lens system to scale down the resulting

pattern, in analogy with the demagnification process employed in conventional optical lithography. The operating conditions for this lens system are investigated in detail, taking into account practical constraints, in order to identify realistic parameters. Simulations of the system using the parameters corresponding to ^{87}Rb BEC have been carried out in order to illustrate the system functionality. With the various patterns used in the simulations, we have shown that the system is indeed capable of generating arbitrary lithography patterns. The proposed lens system has the advantage of flexible control of the pattern demagnification ratio simply by changing the timing of the lens system optical pulses. While the system proposed here is not likely to be used for general purpose lithography, it may enable one to create special purpose patterns on a very scale, with features as small as few nanometers.

ACKNOWLEDGEMENTS

This work was supported by AFOSR Grant #FA9550-10-01-0228, and NSF Grants #DMR-1121262 and #DGE-0801685.

APPENDIX A:

The external potential $V(\vec{r})$ in the GPE equation (1) results from the interaction with the electromagnetic fields. Each of the π and π/2 pulses in Fig. 1 is composed of two counter propagating laser fields parallel to the y axis. We call the field propagating in +y direction $\vec{E}_A$ and the field propagating in –y direction $\vec{E}_B$. Using a semi-classical model, the fields are expressed as:

$$\begin{aligned}\vec{E}_A &= \vec{E}_{A0}\cos(\omega_A t - k_A y + \phi_A) \\ &= \frac{\vec{E}_{A0}}{2}[\exp(i(\omega_A t - k_A y + \phi_A)) + \exp(-i(\omega_A t - k_A y + \phi_A))]\end{aligned} \tag{A1}$$

and

$$\begin{aligned}\vec{E}_B &= \vec{E}_{B0}\cos(\omega_B t + k_B y + \phi_B) \\ &= \frac{\vec{E}_{B0}}{2}[\exp(i(\omega_B t + k_B y + \phi_B)) + \exp(-i(\omega_B t + k_B y + \phi_B))]\end{aligned} \tag{A2}$$

where $\vec{E}_{A0}$ and $\vec{E}_{B0}$ express the magnitude and polarization of the corresponding fields. The Hamiltonian $\hat{H}$ in this case has two parts: $\hat{H} = \hat{H}_0 + \hat{H}_I$. $\hat{H}_0$ represents the internal energy of the condensate and $\hat{H}_I$ represents the interaction energy. Using the electric dipole approximation, the interaction Hamiltonian can be expressed as:

$$\begin{aligned}\hat{H}_I &= \hat{H}_{I_1} + \hat{H}_{I_2} \\ &= -e_0\vec{\varepsilon}.\frac{\vec{E}_{A0}}{2}[\exp(i(\omega_A t - k_A y + \phi_A)) + \exp(-i(\omega_A t - k_A y + \phi_A))] \quad , \\ &\quad - e_0\vec{\varepsilon}.\frac{\vec{E}_{B0}}{2}[\exp(i(\omega_B t + k_B y + \phi_B)) + \exp(-i(\omega_B t + k_B y + \phi_B))]\end{aligned} \tag{A3}$$

where e_0 is the electron charge and $\vec{\varepsilon}$ is the electron position vector for each atom in the condensate. Applying the interaction Hamiltonian to the complete BEC wave function (5) yields

$$\hat{H}_I\left|\psi(x,y,t)\right\rangle = \hat{H}_I\left[\tilde{c}_1(r,t)\left|1\right\rangle + \tilde{c}_2(r,t)\left|2\right\rangle + \tilde{c}_3(r,t)\left|3\right\rangle\right]. \tag{A4}$$

To calculate the interaction Hamiltonian matrix, we note first that $\langle n|\hat{H}_I|n\rangle = 0$, where n is the internal state. Moreover, assuming that $\vec{E}_A$ affects only the $|1\rangle \leftrightarrow |2\rangle$ transition and $\vec{E}_B$ affects only the $|2\rangle \leftrightarrow |3\rangle$ transition, we get $\langle 2|\hat{H}_{I_1}|3\rangle = 0$, $\langle 2|\hat{H}_{I_2}|1\rangle = 0$ and $\langle 1|\hat{H}_I|3\rangle = 0$.

The interaction Hamiltonian can thus be expressed as:

$$\begin{aligned}\hat{H}_I &= \frac{\hbar\Omega_A}{2}\left(|1\rangle\langle 2| + |2\rangle\langle 1|\right)[\exp(i(\omega_A t - k_A y + \phi_A)) + \exp(-i(\omega_A t - k_A y + \phi_A))] \\ &\quad + \frac{\hbar\Omega_B}{2}\left(|2\rangle\langle 3| + |3\rangle\langle 2|\right)[\exp(i(\omega_B t + k_B y + \phi_B)) + \exp(-i(\omega_B t + k_B y + \phi_B))]\end{aligned}, \tag{A5}$$

where the Rabi Frequencies Ω are defined as:

$$\hbar\Omega_A = -e_0 \langle 1|\vec{\varepsilon}.\vec{E}_{A0}|2\rangle = -e_0 \langle 2|\vec{\varepsilon}.\vec{E}_{A0}|1\rangle\,,\ \hbar\Omega_B = -e_0 \langle 2|\vec{\varepsilon}.\vec{E}_{B0}|3\rangle = -e_0 \langle 3|\vec{\varepsilon}.\vec{E}_{B0}|2\rangle\,. \tag{A6}$$

Using the rotating wave approximation [30], Eq. (A5) is simplified to:

$$\begin{aligned}\hat{H}_I = {} & \frac{\hbar\Omega_A}{2}\exp(i(\omega_A t - k_A y + \phi_A))|1\rangle\langle 2| + \frac{\hbar\Omega_A}{2}\exp(-i(\omega_A t - k_A y + \phi_A))|2\rangle\langle 1| \\ & + \frac{\hbar\Omega_B}{2}\exp(-i(\omega_B t + k_B y + \phi_B)|2\rangle\langle 3| + \frac{\hbar\Omega_B}{2}\exp(i(\omega_B t + k_B y + \phi_B))|3\rangle\langle 2|\end{aligned} \tag{A7}$$

Using equation (A7), equation (A4) can be written as:

$$\begin{aligned}\hat{H}_I = {} & \frac{\hbar\Omega_A}{2}\exp(i(\omega_A t - k_A y + \phi_A)\tilde{c}_2(r,t)|1\rangle + \left(\frac{\hbar\Omega_A}{2}\exp(-i(\omega_A t - k_A y + \phi_A)\tilde{c}_1(r,t)\right. \\ & \left. + \frac{\hbar\Omega_B}{2}\exp(-i(\omega_B t + k_B y + \phi_B)\tilde{c}_3(r,t)\right)|2\rangle + \frac{\hbar\Omega_B}{2}\exp(i(\omega_B t + k_B y + \phi_B))\tilde{c}_2(r,t)|3\rangle\end{aligned}\,. \tag{A8}$$

During interaction with the light fields, we have a three component condensate. Each component occupies an independent atomic state. Assuming that the condensate atoms interact only with the atoms in the same state, the complete GPE can be written as:

$$i\hbar\frac{\partial}{\partial t}\psi(r,t) = \sum_{n=1}^{3}\left(-\frac{\hbar^2}{2m}\nabla^2 + U_0|\tilde{c}_n(r,t)|^2 + \hbar\omega_n\right)\tilde{c}_n(r,t)|n\rangle + \hat{H}_I\psi(r,t)\,. \tag{A9}$$

From Eq. (A9) the dynamics of each internal state can be expressed separately as:

$$\begin{aligned}i\hbar\frac{\partial}{\partial t}\tilde{c}_1(r,t) = {} & \left(-\frac{\hbar^2}{2m}\nabla^2 + U_0|\tilde{c}_1(r,t)|^2 + \hbar\omega_1\right)\tilde{c}_1(r,t) + \frac{\hbar\Omega_A}{2}e^{i(\omega_A t - k_A y + \phi_A)}\tilde{c}_2(r,t) \\ i\hbar\frac{\partial}{\partial t}\tilde{c}_2(r,t) = {} & \left(-\frac{\hbar^2}{2m}\nabla^2 + U_0|\tilde{c}_2(r,t)|^2 + \hbar\omega_2\right)\tilde{c}_2(r,t) + \frac{\hbar\Omega_A}{2}e^{-i(\omega_A t - k_A y + \phi_A)}\tilde{c}_1(r,t) \\ & + \frac{\hbar\Omega_B}{2}e^{-i(\omega_B t + k_B y + \phi_B)}\tilde{c}_3(r,t) \\ i\hbar\frac{\partial}{\partial t}\tilde{c}_3(r,t) = {} & \left(-\frac{\hbar^2}{2m}\nabla^2 + U_0|\tilde{c}_3(r,t)|^2 + \hbar\omega_3\right)\tilde{c}_3(r,t) + \frac{\hbar\Omega_B}{2}e^{i(\omega_B t + k_B y + \phi_B)})\tilde{c}_2(r,t)\end{aligned} \tag{A10}$$

In order to simplify equations (A10), the time independence is removed by using the following state transformation:

$$\begin{bmatrix}c_1\\c_2\\c_3\end{bmatrix} = Q\begin{bmatrix}\tilde{c}_1\\\tilde{c}_2\\\tilde{c}_3\end{bmatrix},\qquad Q = \begin{bmatrix}e^{i(\theta_1 t + \phi_1)} & 0 & 0\\ 0 & e^{i(\theta_2 t + \phi_2)} & 0\\ 0 & 0 & e^{i(\theta_3 t + \phi_2)}\end{bmatrix}. \tag{A11}$$

Applying this transformation to Eq. (A10), we have:

$$\begin{aligned}i\hbar e^{-i(\theta_1 t + \phi_1)}\left(\frac{\partial}{\partial t}c_1(r,t) + \hbar\theta_1 c_1(r,t)\right) = {} & \left(-\frac{\hbar^2}{2m}\nabla^2 + U_0|c_1(r,t)|^2 + \hbar\omega_1\right)e^{-i(\theta_1 t + \phi_1)}c_1(r,t) \\ & + \frac{\hbar\Omega_A}{2}e^{i(\omega_A t - k_A y + \phi_A)}e^{-i(\theta_2 t + \phi_2)}c_2(r,t)\end{aligned} \tag{A12a}$$

$$i\hbar e^{-i(\theta_2 t+\phi_2)}\left(\frac{\partial}{\partial t}c_2(r,t)+\hbar\theta_2 c_2(r,t)\right)=\left(-\frac{\hbar^2}{2m}\nabla^2+U_0\left|c_2(r,t)\right|^2+\hbar\omega_2\right)e^{-i(\theta_2 t+\phi_2)}c_2(r,t)$$
$$+\frac{\hbar\Omega_A}{2}e^{-i(\omega_A t-k_A y+\phi_A)}e^{-i(\theta_1 t+\phi_1)}c_1(r,t)+\frac{\hbar\Omega_B}{2}e^{-i(\omega_B t-k_B y+\phi_B)}e^{-i(\theta_3 t+\phi_3)}c_3(r,t) \quad \text{(A12b)}$$

$$i\hbar e^{-i(\theta_3 t+\phi_3)}\left(\frac{\partial}{\partial t}c_3(r,t)+\hbar\theta_3 c_3(r,t)\right)=\left(-\frac{\hbar^2}{2m}\nabla^2+U_0\left|c_3(r,t)\right|^2+\hbar\omega_3\right)e^{-i(\theta_3 t+\phi_3)}c_3(r,t)$$
$$+\frac{\hbar\Omega_B}{2}e^{i(\omega_B t-k_B y+\phi_B)})e^{-i(\theta_2 t+\phi_2)}c_2(r,t) \quad \text{(A12c)}$$

Simplifying Eq. (A12) we get:

$$i\hbar\frac{\partial}{\partial t}c_1(r,t)=\left(-\frac{\hbar^2}{2m}\nabla^2+U_0\left|c_1(r,t)\right|^2+\hbar\omega_1-\hbar\theta_1\right)c_1(r,t)+\frac{\hbar\Omega_A}{2}e^{i((\omega_A+\theta_1-\theta_2)t-k_A y+\phi_1-\phi_2+\phi_A)}c_2(r,t)$$
$$i\hbar\frac{\partial}{\partial t}c_2(r,t)=\left(-\frac{\hbar^2}{2m}\nabla^2+U_0\left|c_2(r,t)\right|^2+\hbar\omega_2-\hbar\theta_2\right)c_2(r,t)+\frac{\hbar\Omega_A}{2}e^{-i((\omega_A+\theta_1-\theta_2)t-k_A y+\phi_1-\phi_2+\phi_A)}c_1(r,t)$$
$$+\frac{\hbar\Omega_B}{2}e^{-i((\omega_B+\theta_3-\theta_2)t+k_B y+\phi_3-\phi_2+\phi_B)}c_3(r,t) \quad \text{(A13)}$$
$$i\hbar\frac{\partial}{\partial t}c_3(r,t)=\left(-\frac{\hbar^2}{2m}\nabla^2+U_0\left|c_3(r,t)\right|^2+\hbar\omega_3-\hbar\theta_3\right)c_3(r,t)+\frac{\hbar\Omega_B}{2}e^{i((\omega_B+\theta_3-\theta_2)t+k_B y+\phi_3-\phi_2+\phi_B)})c_2(r,t)$$

Eliminating the time dependence requires $\omega_A+\theta_1-\theta_2=\omega_B+\theta_3-\theta_2=0$. A convenient option is to choose $\theta_1=\omega_1$ which leads to $\theta_2=\omega_A+\theta_1=\omega_A+\omega_1=\omega_2+\delta_1$ and $\theta_3=\theta_2-\omega_B=\omega_2+\delta_1-\omega_B$. Moreover, we can choose $\phi_A+\phi_1-\phi_2=\phi_B+\phi_3-\phi_2=0$. Consequently Eq. (A13) can be written as:

$$i\hbar\frac{\partial}{\partial t}c_1(r,t)=\left(-\frac{\hbar^2}{2m}\nabla^2+U_0\left|c_1(r,t)\right|^2\right)c_1(r,t)+\frac{\hbar\Omega_A}{2}e^{-ik_A y}c_2(r,t)$$
$$i\hbar\frac{\partial}{\partial t}c_2(r,t)=\left(-\frac{\hbar^2}{2m}\nabla^2+U_0\left|c_2(r,t)\right|^2-\hbar\delta_1\right)c_2(r,t)+\frac{\hbar\Omega_A}{2}e^{ik_A y}c_1(r,t)+\frac{\hbar\Omega_B}{2}e^{-ik_B y}c_3(r,t) \quad \text{(A14)}$$
$$i\hbar\frac{\partial}{\partial t}c_3(r,t)=\left(-\frac{\hbar^2}{2m}\nabla^2+U_0\left|c_3(r,t)\right|^2+\hbar(\delta_2-\delta_1)\omega_3\right)c_3(r,t)+\frac{\hbar\Omega_B}{2}e^{ik_B y}c_2(r,t)$$

Equations (A14) are used to simulate the interaction with laser fields in the spatial domain. The explicit finite difference method is used to discretize the equations for simulation purposes.

References

1. G. Timp, R. Behringer, D. Tennant, J. Cunningham, M. Prentiss, and K. Berggren, Physical Review Letters **69**, 1636 (1992).
2. J.J. Mcclelland, R.E. Scholten, E.C. Palm, and R.J. Celotta, Science **262**, 877 (1993).
3. R. Gupta, J.J. Mcclelland, Z.J. Jabbour, and R.J. Celotta, Applied Physics Letters **67**, 1378 (1995).
4. U. Drodofsky, J. Stuhler, T. Schulze, M. Drewsen, B. Brezger, T. Pfau, and J. Mlynek, Applied Physics B-Lasers and Optics **65**, 755 (1997).
5. W.R. Anderson, C.C. Bradley, J.J. McClelland, and R.J. Celotta, Physical Review A **59**, 2476 (1999).
6. R. Gupta, J.J. McClelland, P. Marte, and R.J. Celotta, Physical Review Letters **76**, 4689 (1996).
7. Z. Liao, M. Al-Amri, and M.S. Zubairy, Physical Review A **88**, 053809 (2013).
8. J.H. Thywissen and M. Prentiss, New Journal of Physics **7**, 47 (2005).
9. Y. Torii, Y. Suzuki, M. Kozuma, T. Sugiura, T. Kuga, L. Deng, and E.W. Hagley, Physical Review A **61**, 041602 (2000).
10. J.E. Debs, P.A. Altin, T.H. Barter, D. Doring, G.R. Dennis, G. McDonald, R.P. Anderson, J.D. Close, and N.P. Robins, Physical Review A **84**, 033610 (2011).
11. H. Muntinga, et al., Physical Review Letters **110**, 093602 (2013).
12. A. Gangat, P. Pradhan, G. Pati, and M.S. Shahriar, Physical Review A **71**, 043606 (2005).
13. C.J. Borde, Physics Letters A **140**, 10 (1989).
14. M. Kasevich and S. Chu, Physical Review Letters **67**, 181 (1991).
15. T.L. Gustavson, A. Landragin, and M.A. Kasevich, Classical and Quantum Gravity **17**, 2385 (2000).
16. T. Muller, M. Gilowski, M. Zaiser, P. Berg, C. Schubert, T. Wendrich, W. Ertmer, and E.M. Rasel, European Physical Journal D **53**, 273 (2009).
17. A.J. Leggett, Reviews of Modern Physics **73**, 307 (2001).
18. S.M. Dickerson, J.M. Hogan, A. Sugarbaker, D.M.S. Johnson, and M.A. Kasevich, Physical Review Letters **111**, 083001 (2013).
19. R. Jannin, P. Clade, and S. Guellati-Khelifa, Physical Review A **92**, 013616 (2015).
20. F. Dalfovo, L. Pitaevskii, and S. Stringari, Journal of Research of the National Institute of Standards and Technology **101**, 537 (1996).
21. E. Giese, A. Roura, G. Tackmann, E.M. Rasel, and W.P. Schleich, Physical Review A **88**, 053608 (2013).
22. H. Ahlers, et al., Physical Review Letters **116**, 173601 (2016).
23. J. Denschlag, et al., Science **287**, 97 (2000).
24. Ł. Dobrek, M. Gajda, M. Lewenstein, K. Sengstock, G. Birkl, and W. Ertmer, Physical Review A **60**, 3381 (1999).
25. N.B. Delone and V.P. Krainov, Phys. Usp. **42**, 669 (1999).
26. D.A. Steck *Rubidium 87 D Line Data*. 2009.
27. M.H. Anderson, J.R. Ensher, M.R. Matthews, C.E. Wieman, and E.A. Cornell, Science **269**, 198 (1995).
28. E.W. Hagley, et al., Physical Review Letters **83**, 3112 (1999).
29. T. Volz, S. Dürr, S. Ernst, A. Marte, and G. Rempe, Physical Review A **68**, 053809 (2003).
30. L. Allen and J.H. Eberly, *Optical resonance and two-level atoms*(Dover, New York, 1987).